A rational approach to improve the overall performances of semitransparent perovskite solar cells by electrode optical management

Antonella Lorusso[a,b], Sofia Masi[c]*, Claudia Triolo[d], Fabrizio Mariano[b], Simone Muia[a], Alessandro Cannavale[e], Yu Duan[f], Marco Anni[a], Maria Luisa De Giorgi[a], Salvatore Patané[g], Olfa Selmi[c], Iván Mora-Seró[c], Stefano De Leo[i]* and Marco Mazzeo[a,b]*

[a]*Department of Mathematics and Physics "Ennio De Giorgi", University of Salento, Via per Arnesano, 73100, Lecce, Italy.*

[b]*CNR NANOTEC-Institute of Nanotechnology, Via Monteroni, 73100 Lecce, Italy.*

[c]*Institute of Advanced Materials (INAM), Universidad Jaume I, Av. Sos Baynat s/n, 12071 Castelló, Spain.*

[d]*Department of Civil, Energy, Environmental and Materials Engineering (DICEAM), Mediterranean University, 89122 Reggio Calabria, Italy.*

[e]*Dipartimento di Architettura, Costruzione e Design (ArCoD), Politecnico di Bari, Via Orabona 4, 70125 Bari, Italy.*

[f]*State Key Laboratory on Integrated Optoelectronics, College of Electronic Science & Engineering, Jilin University, Changchun 130012, P. R. China.*

[g]*Department of Mathematical and Computer Sciences, Physical Sciences and Earth Sciences, University of Messina, 98166 Messina, Italy.*

[h]*Department of Applied Mathematics, 13083-859, Campinas State University, SP, Brazil.*

Corresponding Authors

*Email: masi@uji.es

*Email: deleo@ime.unicamp.br
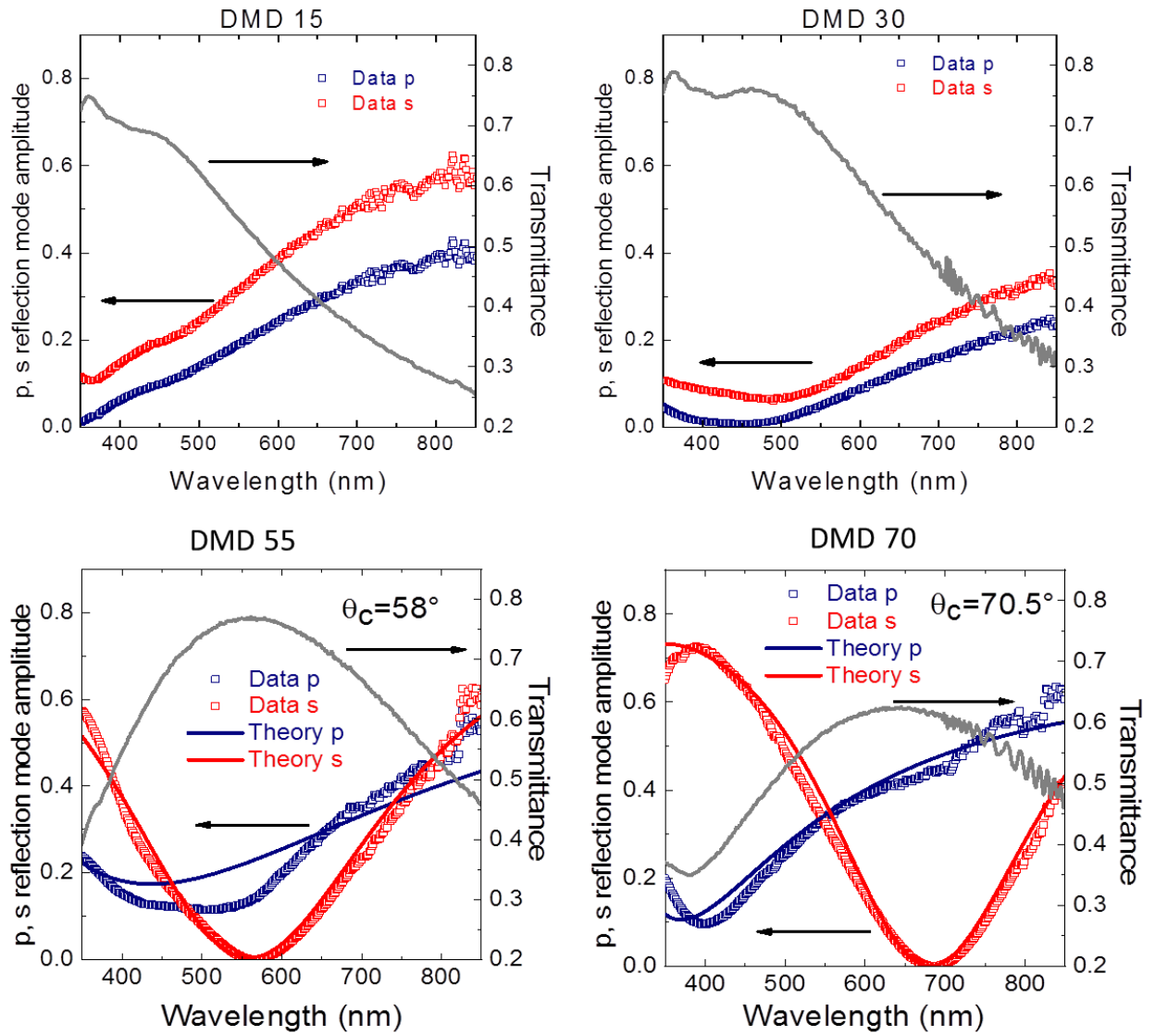
*Email: marco.mazzeo@unisalento.it

Figure S1. Wavelength-dependence of *s* (red dotted curves) and *p* (blue dotted curves) modes at θ_c for DMD15; 30; 55; 70. The grey curves are the transmittance spectra at normal incidence of light. In the case of DMD55 and DMD70 the theoretical p and s curves, as predicted by the analytical model, have been reported as continuous lines.
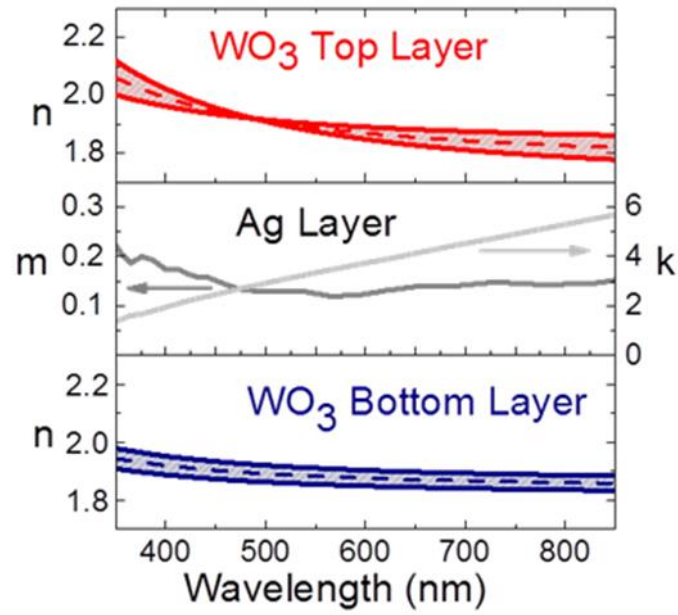
Figure S2. Optical dispersion of DMD layers as a result of Ψ and Δ data fit on DMD*d* electrodes. The colored regions represent the values where the refractive index dispersion curves extracted from all the DMD samples fall. The dashed curves are the average of these values that are then used in the theoretical model.
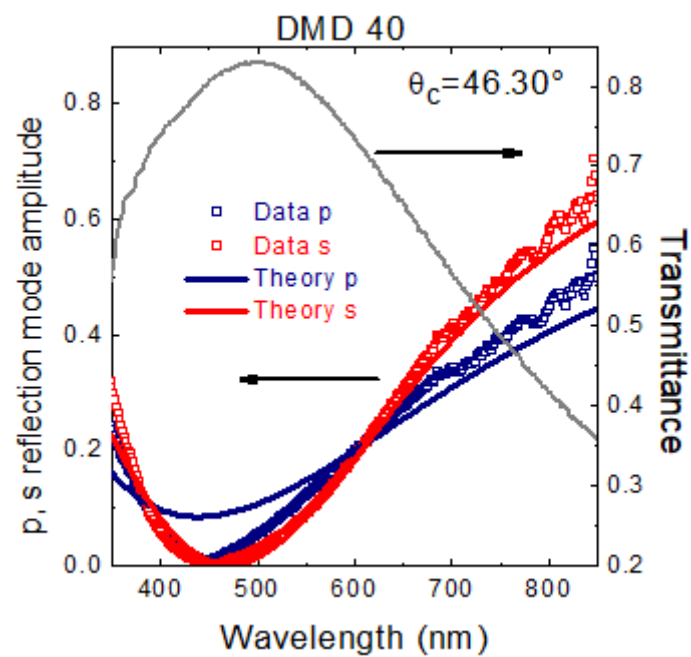
Figure S3. Wavelength-dependence of s (red dotted curves) and p (blue dotted curves) modes at θc and the relative curves (continuous ones) calculated by the analytical model. The grey curve is the transmittance spectrum at normal incidence of light.

Analytical solution of antireflection conditions

We consider the case of four media (thereafter 4M) with the sequence $1_\infty/2/3/4_\infty$, in which the thickness of medium 1 (air) and medium 4 (WO$_3$ bottom) are considered infinite, while medium 2 (WO$_3$ top) and medium 3 (Ag) are thin films with thickness d and t, respectively. In this case, only two thin layers will contribute to the interference, while the bottom layer contributes only by means of the refractive index, resulting in the following expression for reflectance in the 4M-model:

$$R_{4M} = \frac{r_{12}+r_{23}e^{i2\delta_2}+r_{34}e^{i2(\delta_2+\delta_3)}+r_{12}r_{23}r_{34}e^{i2\delta_3}}{1+r_{12}r_{23}e^{i2\delta_2}+r_{23}r_{34}e^{i2\delta_3}+r_{12}r_{34}e^{i2(\delta_2+\delta_3)}} \qquad (S1)$$

Here, r_{ik} is the p or the s Fresnél reflection mode coefficients between the i-th and the k-th layers, while $\delta_k = \frac{2\pi}{\lambda}n_k d_k cos\theta_k$ is the phase related to the optical path in the k-th film whose refractive index and thickness are n_k and d_k respectively, θ_k being the angle of the propagation-ray in the film. In order to validate this model, we plot the reflectance R_{4M} versus the wavelength at different angles of incidence, comparing it with the experimental curves of s and p modes derived by ellipsometric measurements.

The reflection Fresnel coefficients between two media i and j are labelled as $r_{ij} = \frac{q_i-q_j}{q_i+q_j}$ for s mode and $\widetilde{r_{ij}} = \frac{n_j^2 q_i-n_i^2 q_j}{n_j^2 q_i+n_i^2 q_j}$ for p mode, where $q_{i(j)} = n_{i(j)}\frac{2\pi}{\lambda}cos\theta_{i(j)}$, while the transmission coefficients are $t_{ij} = \frac{2q_i}{q_i+q_j}$ and $\widetilde{t_{ij}} = \frac{2n_i n_j q_i}{n_j^2 q_i+n_i^2 q_j}$ for s and p mode, respectively. For a thin film labelled by the index "k" and embedded in between two media with indices "$k-1$" and "$k+$ 1", the reflection coefficient is $R_k = \frac{r_{k-1,k}+r_{k,k+1}e^{i2\delta_k}}{1+r_{k-1,k}r_{k,k+1}e^{i2\delta_k}}$. If the $k+1$-th medium is also a thin film layer, the reflection coefficient is then obtained by the recursive substitution $r_{k,k+1} \rightarrow R_{k+1}$, thus leading to Equation S1. Under the approximation reported in the main text concerning the

refractive index of the dielectric and metal film layers, the following boundary conditions will be defined as follows: $r_{12} = r$; $r_{34} = -r_{23} = e^{-i2\varphi}$, where $\varphi = arctan\sqrt{\frac{k^2+sin^2\theta}{n^2-sin^2\theta}}$. Therefore, the condition $R_{4M} = 0$ leads to the follow equation:

$$r - e^{i2(\delta_2-\varphi)} + e^{i2(\delta_2+\delta_3-\varphi)} - re^{i2(\delta_3-2\varphi)} = 0$$

that can be represented in the Argand plane as the vectorial sum of four complex phasors that close on themselves when $\lambda = \lambda_c$ and $\theta = \theta_c$, when the s mode vanishes. Interestingly, the condition $n_{Ag} \cong ik$ leads to a pure imaginary phase $\delta_3 = i\frac{2\pi kt}{\lambda}cos\theta_3$ thus introducing an exponential damping in the amplitudes of the last two phasors. In the absence of the upper dielectric layer, the phasors obviously do not have the possibility to close on themselves anymore, thus resulting in a highly reflective device (see picture in Figure 1a). We underline that the last term, despite the damping due to the metal layer, cannot be neglected.

The above equation is usually[32] solved at normal incidence and neglecting the last term $re^{i2(\delta_3-2\varphi)}$, where $\varphi = arctan\frac{k}{n}$. This results in the following analytical condition:

$$\frac{1-n}{1+n} + \left[1 - exp\left(-\frac{4\pi kt}{\lambda}\right)\right] exp\left[2i\left(\frac{2\pi nd}{\lambda} - \varphi\right)\right] = 0 \quad (S2)$$

leading to

$$cos\left(\frac{4\pi nd}{\lambda} - 2\varphi\right)\left[1 - exp\left(-\frac{4\pi kt}{\lambda}\right)\right] = \frac{n-1}{n+1} \quad (S3a)$$

$$sin\left(\frac{4\pi nd}{\lambda} - 2\varphi\right)\left[1 - exp\left(-\frac{4\pi kt}{\lambda}\right)\right] = 0 \quad (S3b)$$

From the last equation we get, at $\theta = 0$

$$d = \frac{\lambda}{2\pi n}\varphi$$

and using this solution into Equation S1 we extract t as follow:

$$t = \frac{\lambda}{4\pi k}ln\frac{n+1}{2}$$

7

We obtained the exact analytical solution for all the angle of incidence by solving without any approximations the following equation, which is a better approximation than Equation S2:

$$\mathrm{r} + \exp\left[2i\left(\frac{2\pi d\sqrt{n^2-sin^2\theta}}{\lambda} - \varphi\right)\right]\left[1 - \exp\left(-\frac{4\pi t\sqrt{k^2+sin^2\theta}}{\lambda}\right)\right] = r\,\exp(-4i\varphi)\exp\left(-\frac{4\pi t\sqrt{k^2+sin^2\theta}}{\lambda}\right).$$

Separating the real from the imaginary parts we obtain

$$\cos\left[2\left(\frac{2\pi d\sqrt{n^2-sin^2\theta}}{\lambda} - \varphi\right)\right]\left[1 - \exp\left(-\frac{4\pi t\sqrt{k^2+sin^2\theta}}{\lambda}\right)\right] = r\left[\cos(4\varphi)\exp\left(-\frac{4\pi t\sqrt{k^2+sin^2\theta}}{\lambda}\right) - 1\right] \quad \text{(S4a)}$$

$$\sin\left[2\left(\frac{2\pi d\sqrt{n^2-sin^2\theta}}{\lambda} - \varphi\right)\right]\left[1 - \exp\left(-\frac{4\pi t\sqrt{k^2+sin^2\theta}}{\lambda}\right)\right] = -r\,\sin(4\varphi)\exp\left(-\frac{4\pi t\sqrt{k^2+sin^2\theta}}{\lambda}\right) \quad \text{(S4b)}$$

Squaring the two previous equations and adding member to member we obtain

$$\exp\left(-\frac{4\pi t\sqrt{k^2+sin^2\theta}}{\lambda}\right) = \frac{1-r^2\cos(4\varphi)}{1-r^2} - \sqrt{\left[\frac{1-r^2\cos(4\varphi)}{1-r^2}\right]^2 - 1} = f(r,\varphi) \quad \text{(S5a)}$$

Instead, by dividing Equation S4b by Equation S4a and using Equation S5a we find

$$\frac{2\pi d\sqrt{n^2-sin^2\theta}}{\lambda} = \varphi + \frac{1}{2}arctan\left[\frac{\sin(4\varphi)f(r,\varphi)}{1-\cos(4\varphi)f(r,\varphi)}\right] = g(r,\varphi) \quad \text{(S5b)}$$

From Equation S5a and b we then get the analytical solution for t and d at any θ namely:

$$t = \frac{\lambda}{4\pi}\frac{\ln[1/f(r,\varphi)]}{\sqrt{k^2+sin^2\theta}} \quad \text{(S6a)}$$

$$d = \frac{\lambda}{2\pi}\frac{g(r,\varphi)}{\sqrt{n^2-sin^2\theta}} \quad \text{(S6b)}$$

The results are calculated and reported in Figure S4, where λ_c (blue curves) and the dielectric layer thickness d (red curves), are plotted against the incidence angle for metal thickness ranging from 11nm to 15nm, showing clearly that the 4M model matches very well with the experimental data (we underline that the 14nm thick Ag layer has been deposited within an incertitude of 1nm). Moreover, it is clear that the antireflection conditions can be finely tuned in the whole visible range just by tuning the dielectric thickness.
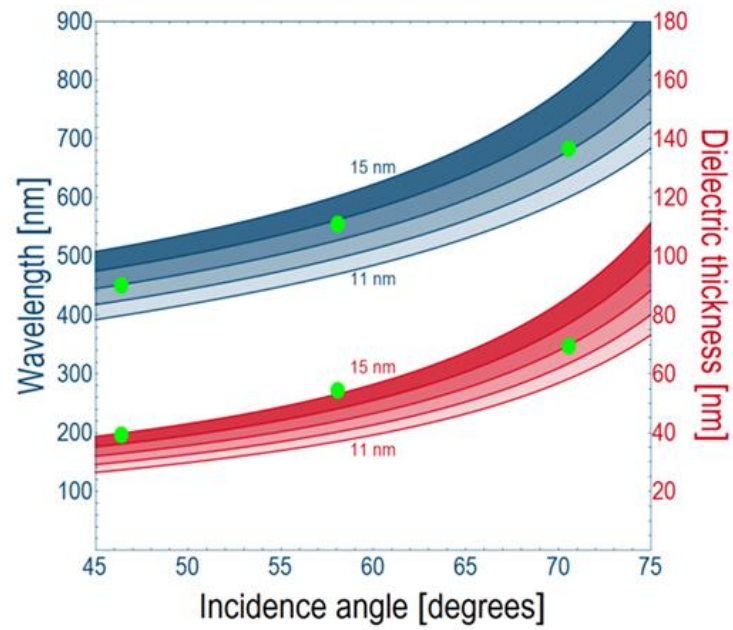
Figure S4. Plot of critical wavelength (bluish curves) and dielectric thickness (reddish curves) vs. the angle of incidence for different Ag thickness from 11 to 15nm with 1nm step, as calculated from Eq.2 of main text and Eq.S6a,b. Dots represent experimental data corresponding to DMD40, DMD55, DMD70.
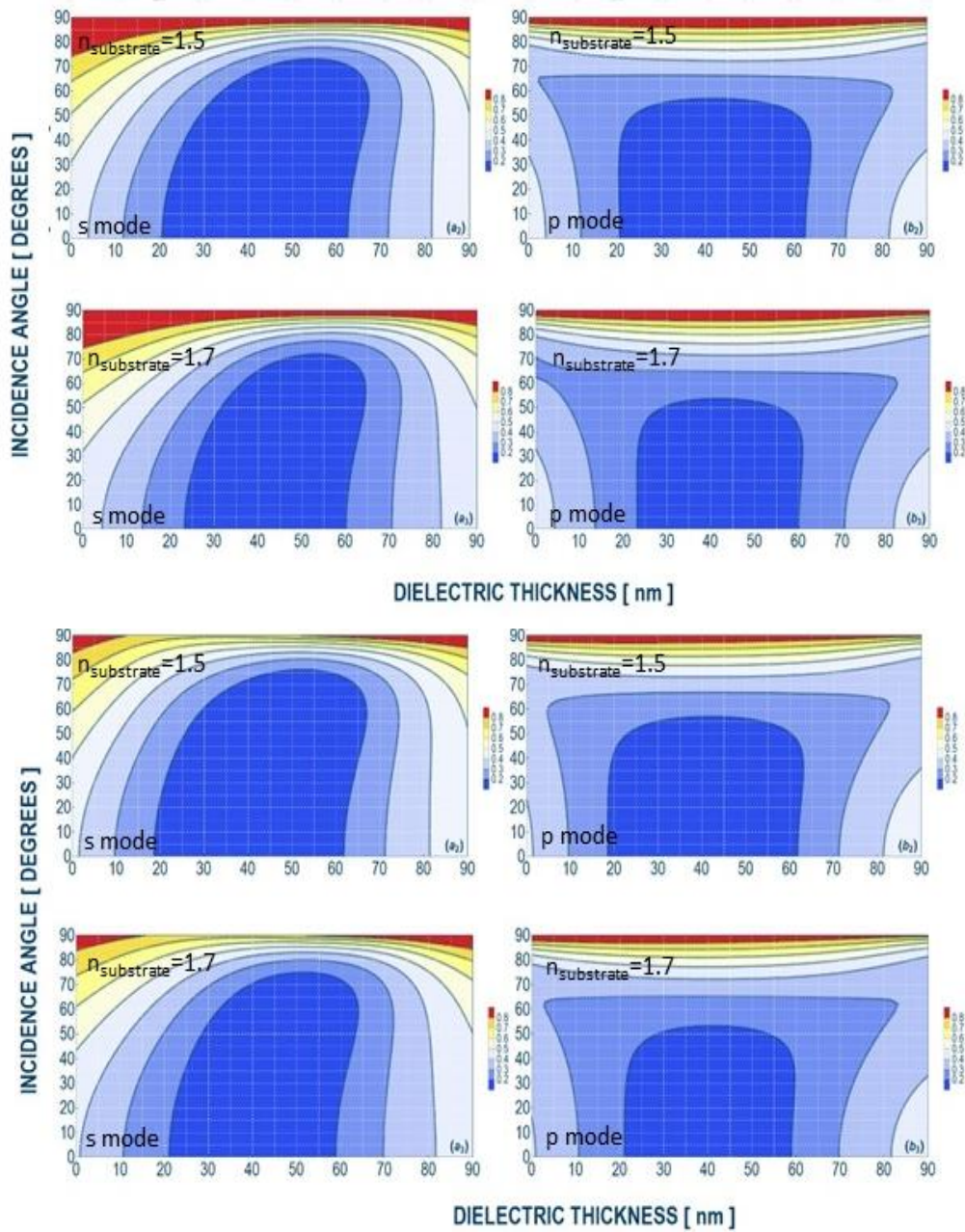
Figure S5. AVR maps of *s* and *p*- intensity reflection modes as a function of the dielectric thickness and the angle of incident light for a DMD deposited on Glass (refractive index 1.5) and Organic substrate as in the Solar Cell (refractive index 1.7). top figure) light incoming from the top; bottom figure) light incoming from the substrate side.
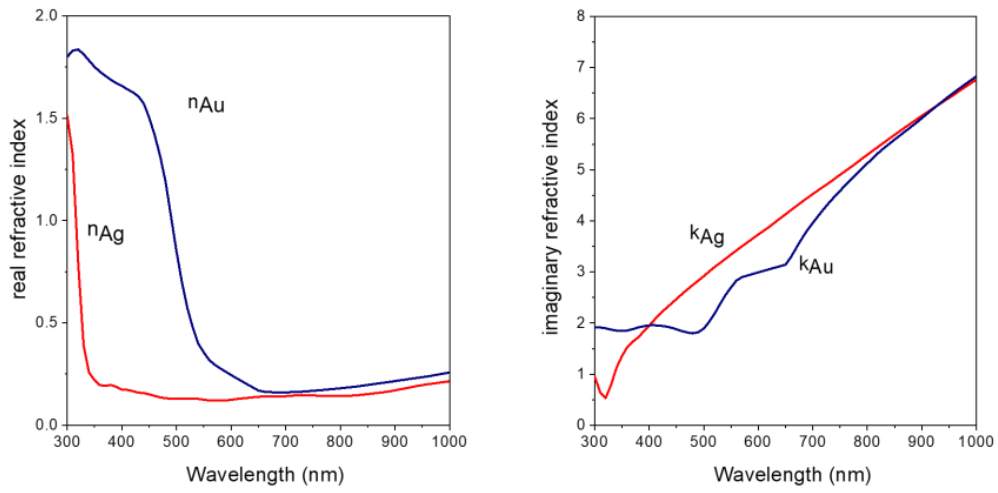
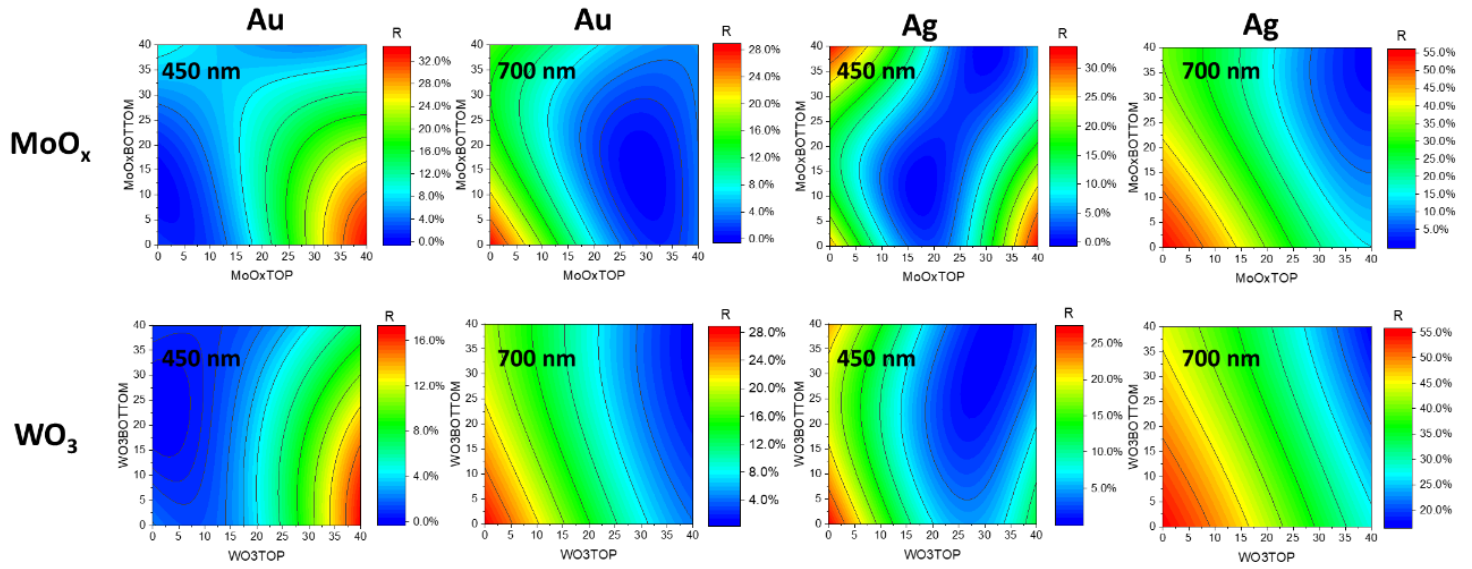**Figure S6.** Optical dispersion curves of Ag and Au.

Figure S7. Maps of reflectance intensity (at normal incidence) vs. bottom and top dielectric thickness for D/Au(10nm)/D and D/Ag(14nm)/D, where D stays for WO₃ and MoO$_x$, at two wavelength values (450nm and 700nm). As we can see, at 700nm, the MoO$_x$/Au/MoO$_x$ architecture leads to a minimum reflectance (blue region) with an asymmetric structure, i.e. 15nm/Au/35nm. Nevertheless, this configuration does not lead to a minimum reflectance value at shorter wavelengths (i.e. 450nm): here the minimum value corresponds to a reversed configuration (10nm/Au/5nm). These findings do not depend on the dielectric layers used (see WO₃ based devices simulations). On the contrary, with Ag in place of Au, antireflection conditions are achieved with the same symmetric architecture configuration, namely 40nm/Ag/40nm, in the whole spectra range.
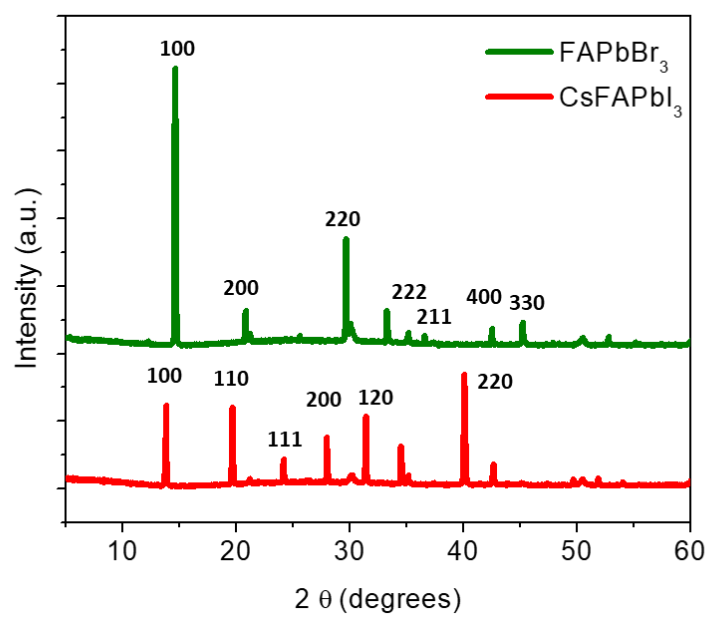
Figure S8. X-ray diffraction pattern of the CsFAPbI$_3$ and FAPbBr$_3$ films.
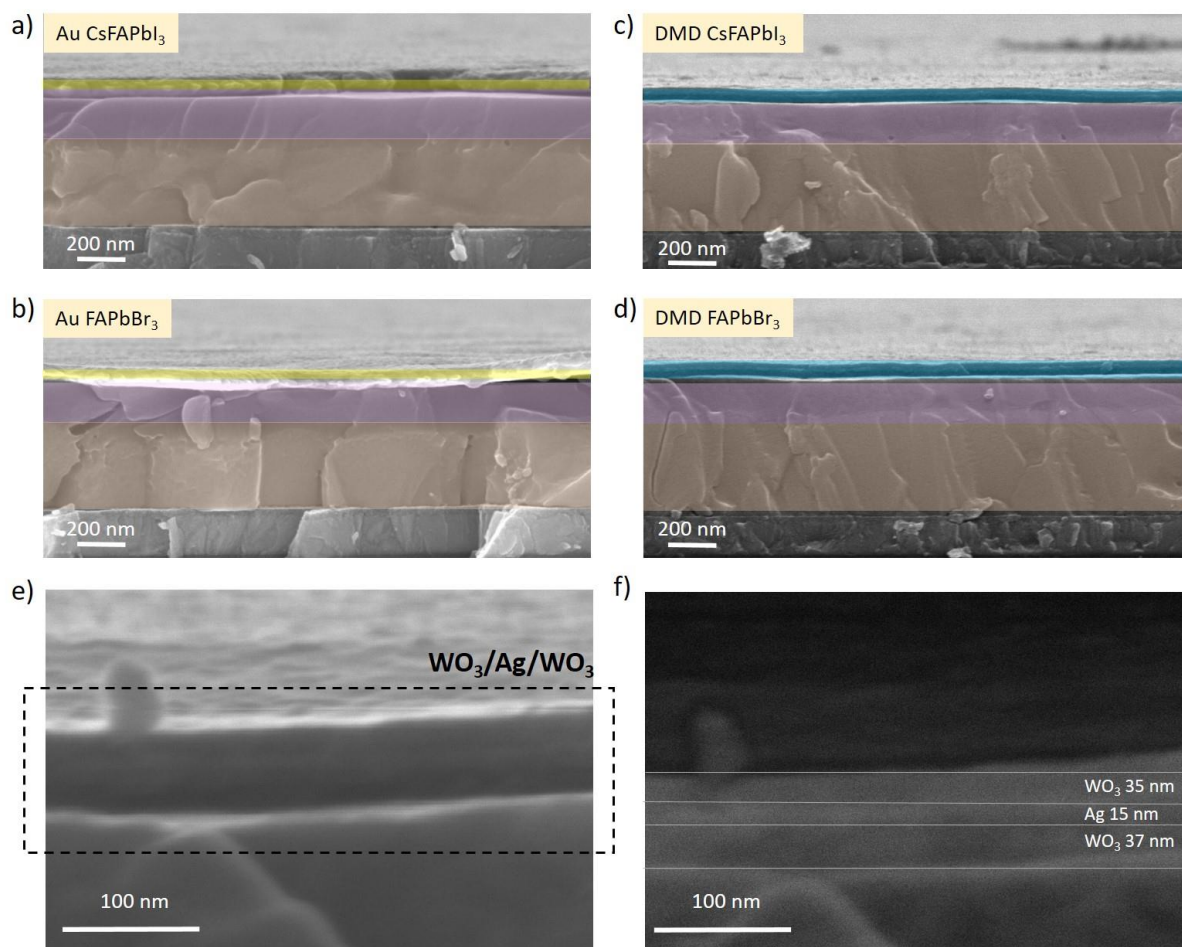
Figure S9. a)-d) Cross-section SEM images of the perovskite solar cells with Au electrode (on the left) and with DMD40 electrode (on the right). e) Cross section zoom-in SEM image of the DMD40 electrode, and f) COMPO mode images highlighting the 3 layers (top WO_3, Ag and bottom WO_3).
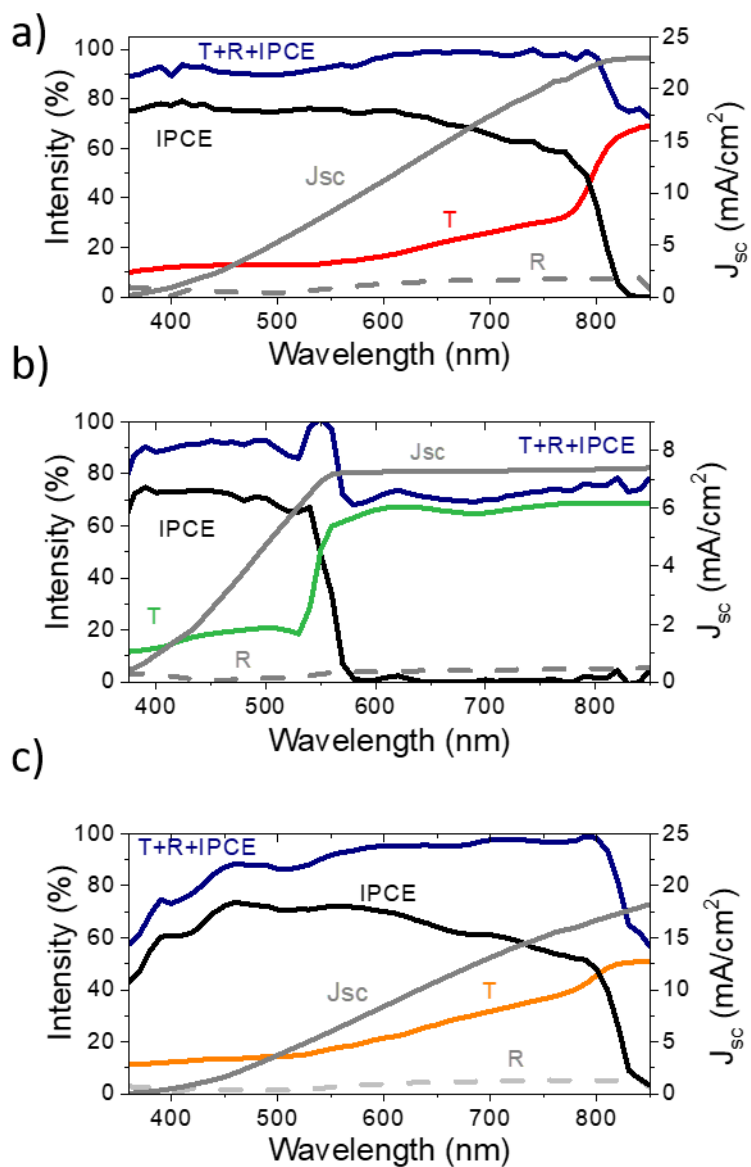
Figure S10. Integrated Current Density (J_{sc}), Internal-photon-to-current-efficiency (IPCE), Transmittance (T), diffused Reflectance (R) and photon-balance check measurements (T+R+IPCE) for a) DMD40-CsFAPbI$_3$, b) DMD40-FAPbBr$_3$ and c) DMD40-FAPbI$_3$
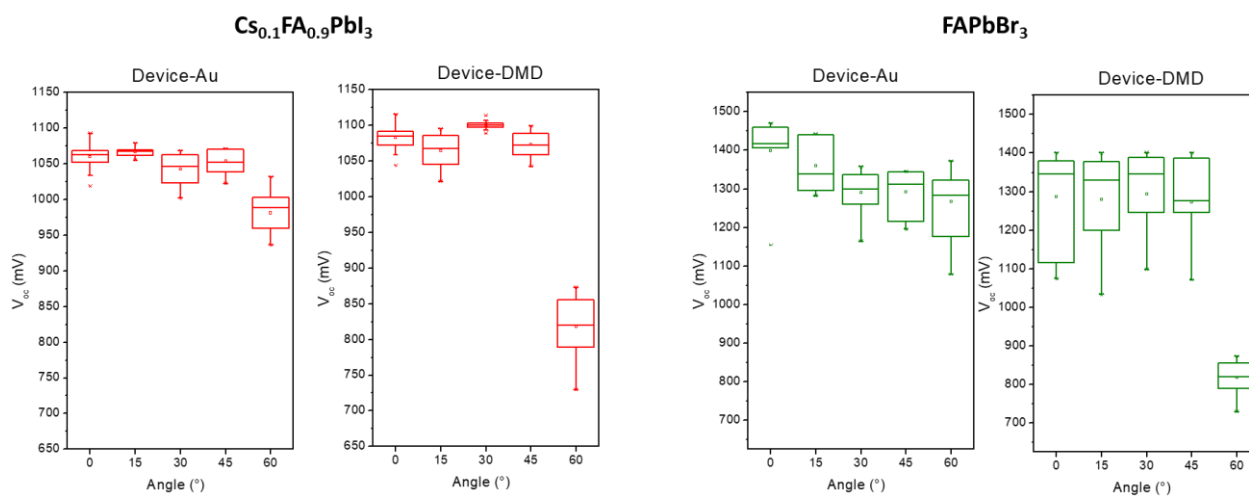
Figure S11. Open circuit Voltage (V_{oc}) versus angle of incidence of Device-30nmAu (left) and

Device-DMD40 (on the right) for CsFAPbI$_3$ and FAPbBr$_3$ perovskites.

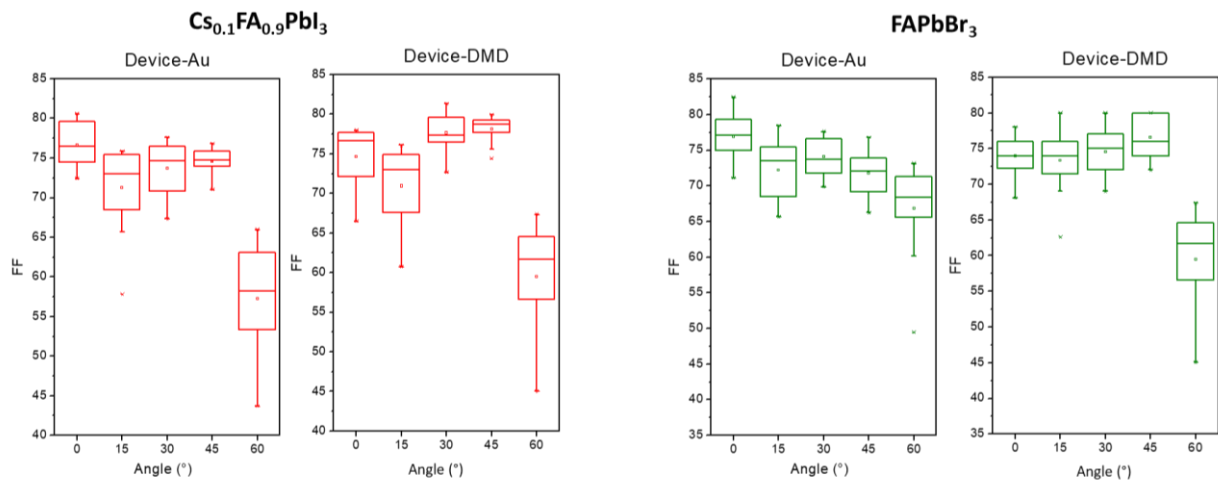**Figure S12.** Fill Factor (FF) versus angle of incidence of Device-30nmAu and Device-DMD40 for CsFAPbI$_3$ and FAPbBr$_3$ perovskites.
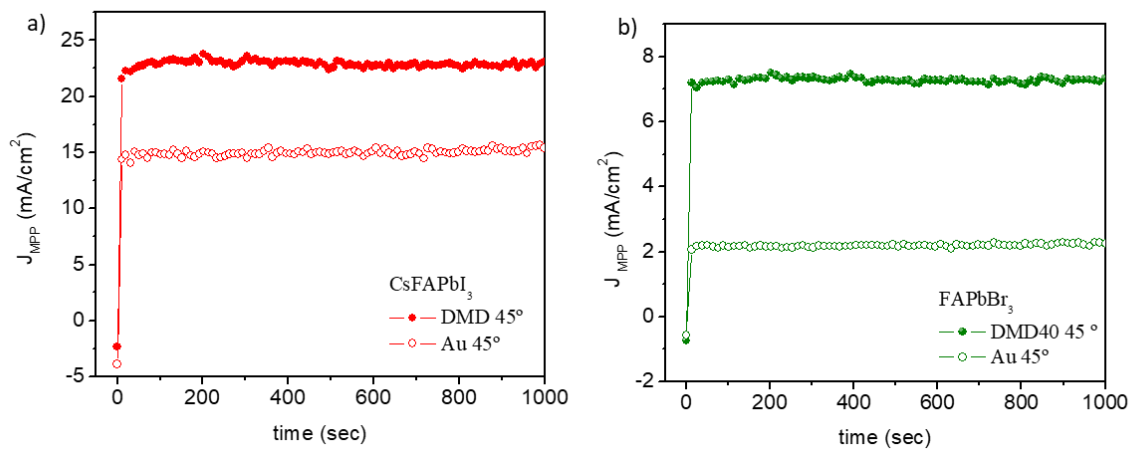
Figure S13. Steady state current at maximum power point (J_{MPP}) for Device-DMD40 and Device-30nmAu at the angle of incidence of 45° for CsFAPbI$_3$ and FAPbBr$_3$ perovskites.
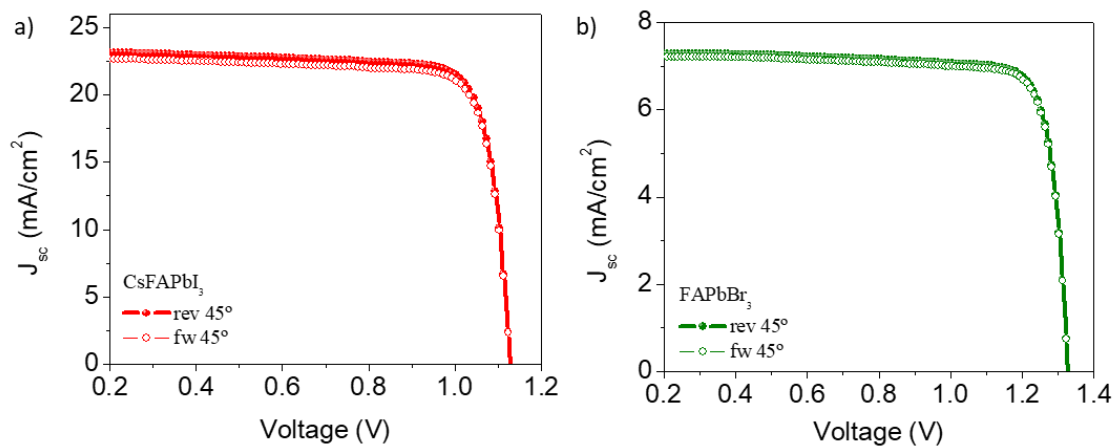
Figure S14. Forward and Backward J/V curves for Device-DMD40 at the angle of incidence of 45°.

	J_{sc} (mA/cm^2)	V_{oc} (V)	FF	PCE (%)
DMD40 rev CsFAPbI$_3$	23.1	1.101	80	20.3
DMD40 fw CsFAPbI$_3$	22.6	1.100	79	19.6
DMD40 rev FAPbBr$_3$	7.3	1.350	79	7.8
DMD40 fw FAPbBr$_3$	7.2	1.350	78	7.4

Table S1. Figures of merits for Device-DMD40 at the angle of incidence of 45° (scan from 1.2V to -0.02 V and *viceversa*).

Figure S15. V_{oc}, J_{SC} and FF versus AVT of the DMD40-CsFAPbI$_3$ (red filled star dot), DMD40-FAPbI$_3$ (red empty star) and DMD40-FAPbBr$_3$ (green filled star) devices compared with literature (b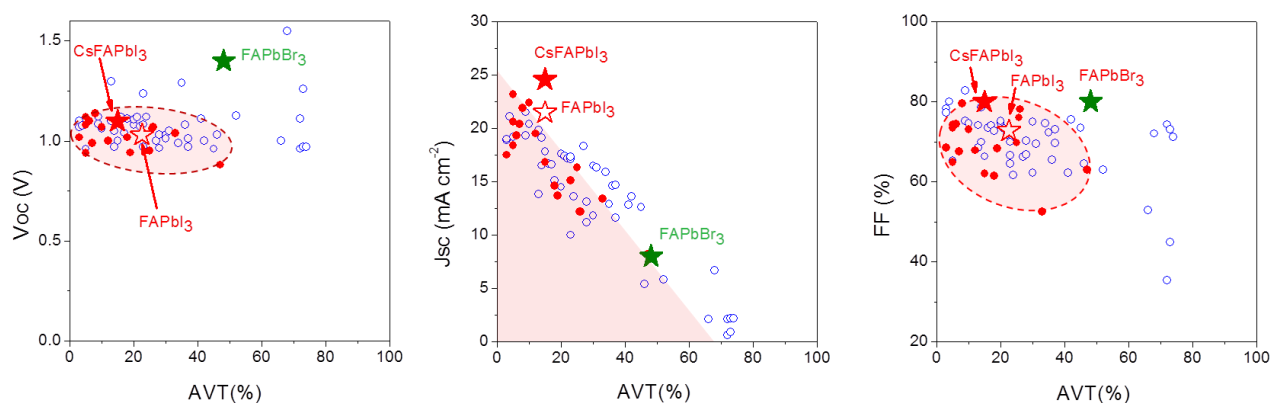lue open dots refer to mixed perovskites devices while red dots refer unmixed ones). Reddish zones represent the reported values as from literature for unmixed perovskites-based devices.

EXPERIMENTAL METHODS

DMD structures: All the materials of the DMDs structures realized (WO_3; Ag) were deposited sequentially by thermal evaporation in a high vacuum chamber (10^{-6} mbar) at a rate of 0.5-1 Å/s on ITO-coated glass substrates. The substrates were sonicated in acetone for 10min and then in isopropyl alcohol before being dried with nitrogen, and finally cleaned by UV ozone treatment.

Optical analysis: The measurements were performed by using variable angle spectroscopic ellipsometer (Model: M2000-XI, J. A. Woollam Co.) in the wavelength range from 300nm to 1000nm varying the incident angle θ from 45° to 70°, while the data are analysed by CompleteEASE spectroscopic ellipsometry software. Since the growth of Ag and WO_3 layers is affected by the layer surface on which they are deposited, we have extracted more realistic optical dispersions by analysing the ellipsometric data carried out after growing the films layer by layer on glass: that is Glass/WO_3 (D) Glass/WO_3/Ag (DM) and Glass/WO_3/Ag/WO_3 (DMD). Therefore the optical dispersion data previously obtained in D and DM are used as initial inputs to find the real optical dispersions and thickness of all the employed layers that are able to fit the ellipsometric data of the final DMD architecture. In order to fit the ellipsometric data, for the WO3 layer refractive index dispersions we used the Cauchy model following the expression $n(\lambda)=A+B/\lambda^2 +C/\lambda^4$, while for the metal layer we used the Drude-Lorentzian model in the Maxwell- Garnett approximation to take into account a possible percolation of metal into the dielectric layer.

Solar cells materials: Lead iodide (98%, from TCI), formamidinium iodide (98%, from Greatcellsolar), 2-propanol (99.7% from Carlo Erba), ethanol (96%) and acetone (99.25%) from PanReac, hydrochloric acid (37%), dimethylformamide (anhydrous 99.9%), clorobenzene (anhydrous 99.8%), acetonitrile (anhydrous 99.8%), diethylether (anhydrous 99.8%), 4-tert-butylpiridine (96%), zinc powder (99.995%) and lithium bis(trifluoromethylsulfonyl)imide (99.95%) from Sigma Aldrich, while 2,20,7,70-tetrakis [N,N-di(4-methoxyphenyl)amino]-

9,90-spirobifluorene (spiro-OMeTAD 99%) from Feiming chemical limited, and SnO_2 colloid precursor from Alfa Aesar (15% in H_2O colloidal dispersion). Indium tin oxide (ITO) coated glass substrates (Pilkington TEC15, ~ 15 Ω/sq).

Solar cell fabrication: Indium tin oxide (ITO) coated glass are etched with Zn powder and 6 M hydrochloric acid and followed by 15 min of ultrasonication cleaning with deionized water, acetone, and isopropanol. The 2.65wt% of colloidal SnO_2 is deposited, after an UV-ozone treatment for 20 min, by spin-coating at 3,000 rpm for 40s, and annealed at 150 °C for 30min. Before the perovskite deposition, SnO_2 substrates are treated with UV-Ozone for 20min to improve the wettability of the perovskite. The $FAPbI_3$ solution is spin-coated at 5,000 rpm for 17s and 400μL of diethyl ether solution is dropped on the spinning substrate at 9th second. The substrate is then annealed at 100 °C for 1 min and 165 °C for 10min. The $CsFAPbI_3$ perovskite solution is prepared by dissolving 26mg of CsI (0.1mmol) 461mg of PbI_2 (1mmol) and 172mg of FAI (1mmol), 96.30μL of N-Methyl-2-pyrrolidone (NMP, 1mmol) in N,N-dimethylformamide (DMF, 590.71 μL) and heated at 60 °C. Then, a solution of butilammonium bromide in isopropanol (3mg/ml) is deposited at 5,000rpm for 30s. The $FAPbBr_3$ is prepared by dissolving 62.5mg of FABr (1mmol) + 196.4mg $PbBr_2$ (1.07mmol) in 375 μl DMF + 135 μl DMSO and spin coated at 3,000rpm for 30s. 300μl of toluene as antisolvent is dropped at 10th second. Finally, the perovskite is annealed at 90 ℃ for 10min. Subsequently, the Spiro-OMeTAD solution (72.3 mg/mL in 1 mL chlorobenzene and followed by the addition of tert-butyl pyridine 28.8 μL and Lithium bis(trifluoromethyl sulfonyl) imide 17.5μL of a 520mg/ml solution in acetonitrile) is deposited by spin coating at 4,000rpm for 35s. Finally, 30nm of the gold counter electrode or WO_3 (40nm)/Ag (15nm)/WO_3 (40nm) are deposited using a thermal evaporator. Note that, the perovskite thin film and Spiro-OMeTAD deposition are carried out at ambient atmosphere conditions.

Solar cell characterization: The current-voltage (J-V) curves are measured using a Keithley 2612 source meter under AM 1.5 G (1000 Wm^{-2}) provided by a Solar Simulator Abet, Xenon

short-arc lamp Ushio 150W, in air at a temperature around 25°C and without encapsulation. Each curve is generated using 123 data points from a starting potential of 1.2 V to a final potential of -0.02 V (reverse scan; viceversa for the forward scan) using a scan rate of 10 mVs^{-1}. The active area of the cell is 0.121 cm^2. The photovoltaic performance at different angles are measured by changing the inclination of the device by means of a support with different orientation. The angles are measured by the means of a graduated goniometer and a tip parallel to the normal direction of the plane device: (0º, 15º, 30º, 45°, 60º are the angles between the source light direction and the normal axis of the device). The characterization has been carried out with light entering from electrode side for both Au and DMD based cells.

The *transmittance* spectra were obtained using a UV/Vis absorption spectrophotometer (Varian, Cary300) in the wavelength range of 200-850 nm. The absolute reflectance has been measured with an integrated sphere Labsphere DRA-CA-30I situated inside the spectrophotometers sample compartment.

X-Ray Diffraction (XRD): The X-ray diffraction (XRD) pattern is registered by a diffractometer (Bruker AXS, D8 Advance) equipped with a primary monochromator of Ge. Measurements were taken using Cu Kα radiation (wavelength of I = 1.5406Å) over a 2θ range between 5° and 70° with a step size of 0.02°.

Incident photon to current efficiency (IPCE): IPCE measurements were performed with a QEPVSI-b Oriel measurement system, by using a Xenon lamp with a monochromator Oriel Cornestone 130. Before measurement, calibration was done using a reference photodiode of silicon and each measurement is obtained using TRACQ BASIC software. Finally, IPCE scans were taken from 350 nm to 850 nm with increment of 10 nm.

Scanning Electron Microscopy (SEM): The cross section of the samples (FTO/SnO$_2$/CsFAPbI$_3$ or FAPbBr$_3$/spiro-OMeTAD/Au or DMD40) were carried out with a field emission scanning electron microscope FEG-SEM JEOL 3100F operated at 5kV.